Society of Petroleum Engineers

SPE-181654-MS

Source Parameters of Repeating Microseismic Events During Hydraulic Fracturing Operations

Kevin Chao and German A. Prieto, Earth Resources Laboratory, MIT; Jing Du, Total E&P

This paper was prepared for presentation at the SPE Annual Technical Conference and Exhibition held in Dubai, UAE, 26-28 September 2016.

Abstract

A complete microseismic event catalog with accurate source parameters can lead to a more thorough understanding of the temporal and spatial variation of stress during hydraulic fracturing operations. We detect, locate, and characterize repeating microseismic events by determining their source parameters such as magnitude, stress drop, and rupture size, and analyze the continuous microseismic data recorded by one borehole array during a hydraulic injection process. With an existing microseismic event catalog, we first re-calculate accurate moment magnitude and stress drop using estimated source spectra for all events. In addition, we detect and locate smaller events that show only clear S-wave arrivals using a template-matching and waveform cross-correlation technique to identify repeating microseismic activities. We obtain the template waveforms by stacking similar waveforms from repeating microseismic families. Among the ~1300 re-computed events, the moment magnitude calculated from the *P*- and *S*-waves spectra analysis ranges between Mw −1.5 and −3.5. These events are located within a 700m by 200m area as much as 250m deep. Our results indicate a fault radius on the order of one to six meters and fault slip between 10_{-5} to 10_{-3} cm around the fracturing region. In addition, using a matching-filter technique, we detect and locate low signal-to-noise ratio events that we consider repeating microseismic events. Our observations indicate that most repeating families occur at later times in shallower layers. Also, we observe a strong magnitude dependence of the stress drop, with larger magnitude events exhibiting significantly greater stress drops than smaller ones, in contrast to tectonic events in California or Japan. Our estimations of source parameters provide a key to a more in-depth understanding of the relationship between hydraulic fracturing and microseismic activity.

Introduction

During hydraulic fracturing operations, geophones are installed in neighboring observation wells to monitor microseismic events induced by the injection of fracturing fluid (Warpinski, 2009). To obtain the location of microseismic events, the conventional method adapts *P*-wave polarization (i.e., particle motion for incident angle) and *S*-*P* travel time difference (i.e., hypocenter distance and depth) methods (Eisner et al., 2010; Fischer et al., 2008; Warpinski, 2009). The magnitudes of events are determined from the maximum amplitude of *S*-waves. Since the magnitude of induced microseismicity is very small (i.e.,

moment magnitudes range from −2 to −6) (Albright and Pearson 1982; Gibowicz et al., 1991) and normally recorded by a single vertical array in a nearby area (e.g., within a few thousand meters), the accurate source parameters of micro events can be obtained for only events with clear *P*- and *S*-wave arrivals. Although studies have proposed a number of approaches to improving the accuracy of locating these events (Anikiev et al., 2014), most events with only an *S*-wave arrival will be excluded because of their lack of clear P-wave arrivals. Thus, to more accurately and thoroughly interpret the faulting geometry and the mechanism of the hydraulic fracturing process, we must constrain the location of events without clear *P*-wave arrivals and obtain accurate source parameters (e.g., event location, stress drop, and fault dimension) of the microseismic catalog.

Many studies of natural earthquakes have observed repeating earthquakes that occur periodically in the same area of a fault with highly identical *P*- and *S*-waves but different amplitudes (Nadeau and Johnson, 1998). The observations of repeating earthquakes are useful for studying temporal variation in the fault zone (Uchida et al., 2016; Igarashi et al., 2003) and rebuilding a highly complete earthquake catalog by adding as many as ten times the number of small magnitude events, such as foreshocks and aftershock sequences (Peng and Zhao, 2009). For comparison, few studies have focused on the repeating events for induced seismicity during the hydraulic fracturing process (Eisner et al., 2006). A recent study has applied a similar technique to the hydraulic fracturing dataset to detect microseismicity with similar waveforms and *S*-*P* travel time differences (Stuermer et al., 2012), but whether or not observations of repeating microseismic events can be used to detect small magnitude-induced events remains unclear.

In this study, we identify repeating microseismic events with a waveform cross-correlation technique during hydraulic fracturing operations and adapt the matching-filter technique (Caffagni, 2016) to detect more repeating events that were originally not included in the catalogs. We also calculate accurate source parameters of repeating microseismicity such as location, moment, moment magnitude, stress drop, and fault zone dimensions. With such information, we can constrain the location of events with only *S*-wave arrivals.

Data

We analyzed a three-hour continuously recording seismic dataset during hydraulic fracturing operations in Argentina from events recorded by one borehole array located at a ~2,500 m depth from the surface and ~1,000 meters apart from the induced seismicity active area (Figure 1). The vertical borehole array consisted of 24 three-component geophones (12 levels double stacked) with a 4,000 Hz recording sampling rate (Figure 1b). The dataset used in this study includes more than five hours of continuously recorded waveforms and event waveforms from the catalog based on the triggering threshold of amplitude. The catalog of triggered events includes magnitude and location information for ~1,300 microseismic events with clear *P*- and *S*-wave arrivals. Although the dataset also includes surface arrays, we analyze only the borehole dataset because the magnitude of its induced microseismicity is subtle (magnitude less than −1) and a large percentage of the events were not recorded by the surface array. To organize the dataset, we first read the original data, rotated the X and Y components to the E-W and N-S directions based on the tool angles of each receiver obtained from perforation data, and converted the seismograms from voltage to velocity and displacement for further analysis.

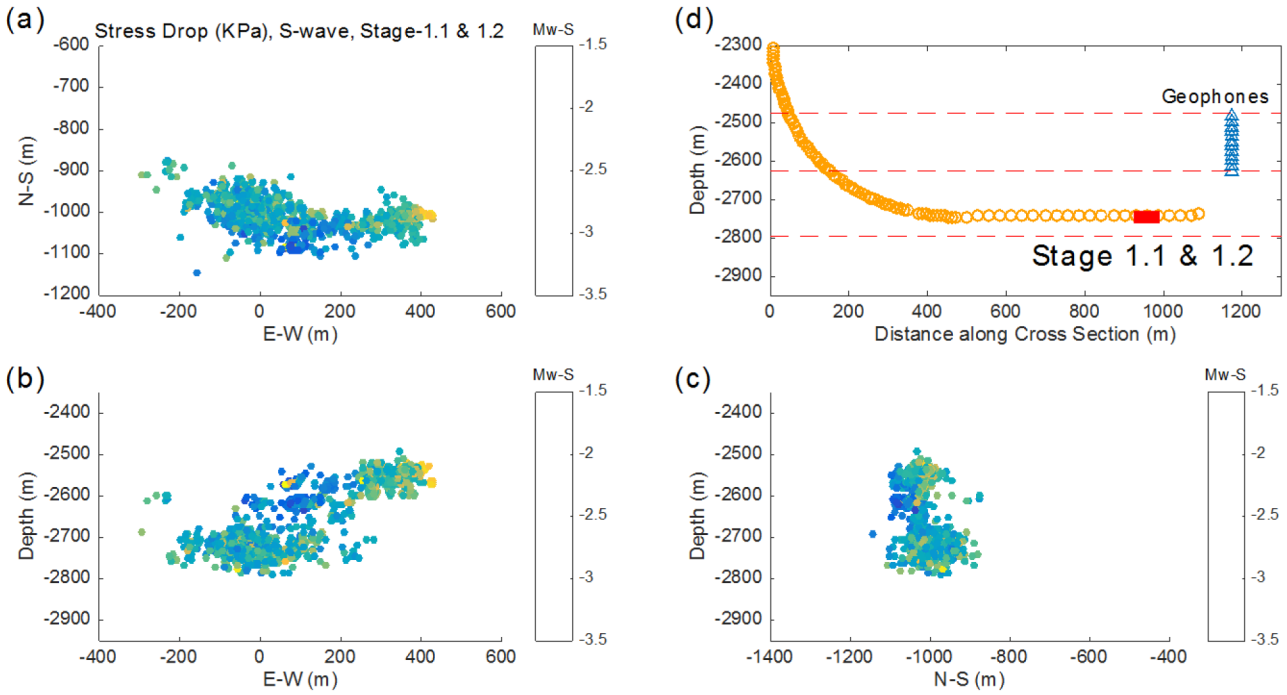

Figure 1—(a) Study area in the map view, (b and c) the cross-section view, and (d) the microseismic monitoring geometry

Methods and Results

Locations

To compare the locations with the triggered events catalog, we re-locate ~200 events with a high signal-to-noise ratio of *P*- and *S*-waves. To locate each event, we obtain the *S*-*P* time difference of all 12 stacked receivers based on the waveform cross-correlation among the arrival phase of the *P*- and *S*-waves. By grid-searching the minimum *S*-*P* time difference of the observed and theoretical time with the 1-D velocity model, we determine the distance between the receiver and the event hypocenter. Next, we estimate the *P*-wave particle motion and identify the incident angle of each event. Finally, we combine the distance and the incident angle and obtain the best source locations. The results show that both newly calculated locations and catalog locations are similar but that their differences fall within the error ranges. Thus, for the calculation of moment magnitude in the next step, we use the catalog locations for a closer comparison.

Calculation of corner frequency (f_c) and amplitude spectra (Ω_0)

To obtain the moment, moment magnitude (Mw), stress drop, and fault dimension, we compute the corner frequency (f_c) and amplitude spectra (Ω_0) for the *P*- and *S*-waves. For detailed calculation steps, we first convert the velocity seismogram to displacement seismograms (Figures 2a-b), calculate the amplitude spectrum via a tapered FFT, and then from all 12 records, obtain the stacked amplitude spectrum (bold red line in Figures 2c-d). Next, we compute the best fitting function between the stacked spectrum (red line in Figures 2c-d) and a simple omega-squared source model (Brune, 1970, Prieto, 2007; Kane et al., 2011) by assigning an assumed f_c (i.e., inverted green triangle in Figures 2c-d). The final f_c for each component is obtained by the best fitting function (Shearer 2009; Stein and Wysession, 2009). Once we obtain an individual f_c for each of the three components of the *P*- and *S*-waves, we calculate the final f_c and Ω_0 (i.e., the flat blue line located to the left of f_c) based on the average of the three-component observations. For each event, we obtain f_c and Ω_0 for the *P*-wave and the *S*-wave.

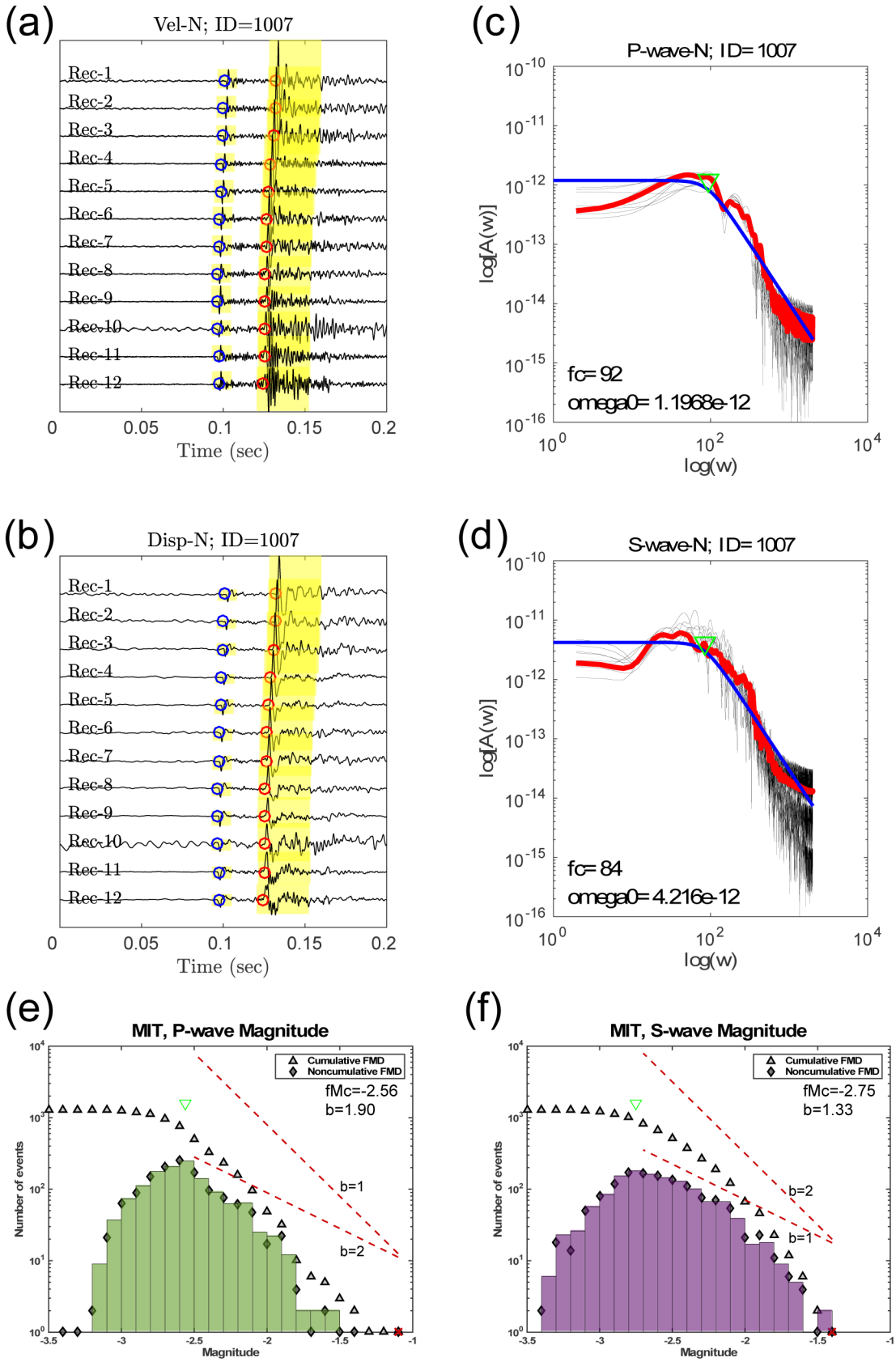

Figure 2—Example of velocity (a) and displacement (b) seismograms and spectra for *P*- (c) and *S*-waves (d). The b-value calculation for the *P*-wave (e) and the *S*-wave (f).

Next, we compute the moment (M_0), the moment magnitude (M_w), and the stress drop ($\Delta\sigma$) for *P*- and *S*-waves with the following equations. The moment (M_0, N-m) is calculated by

$$M_0 = \frac{4\pi\rho c^3 r\Omega_0}{U_{\phi\theta}}, \quad (1)$$

where ρ is the density (2,600 kg/m^3), c is the *P*- or *S*-wave velocity (3.4 or 2.1 *km/s*), r is the distance from the source (m), Ω_0 is the amplitude spectra (the amplitude with the frequency less than f_c), and $U_{\#\theta}$ is the radiation pattern (0.52 or 0.63 for *P*- or *S*-wave). Then the moment magnitude (M_w) can be determined by

$$\mathrm{M_w} = \frac{2}{3}[\log_{10}\mathrm{M_0} - 9.1]. \quad (2)$$

The stress drop ($\Delta\sigma$, Mpa) is defined as

$$\Delta\sigma = \frac{7}{16}\left(\frac{f_c}{\kappa\beta}\right)^3 M_0, \quad (3)$$

where f_c is the corner frequency, κ is a constant (0.32 and 0.21 for the *P*- and *S*-waves, depending on the assumed rupture velocity), and β is the *S*-wave velocity (2.1 *km/s*). In addition, we calculate the fault radius (r, meter), $r = \kappa\beta/f_c$, and the slip ($\overline{D}$, meter), $\overline{D} = M_0/\mu A$, where μ is the shear modulus ($\mu = \rho\beta^2$) and A is the area of the fault ($A = \pi r^2$). Our calculation of M_w for the *P*- (Figure 2e) and *S*-waves (Figure 2f) show ranges between −1.5 and −3.5. The b-value of M_w for the *P*-wave (i.e., b=1.90) is higher than that of the *S*-wave (i.e., b=1.33). Observations of the magnitudes are similar to the magnitudes in the existing catalog.

Observations show that the stress drop depends on the magnitude for Stage 1.2. The larger magnitude events exhibit larger stress drops by as much as 10 KPa (Figure 3). The stress drop for all shallower events (i.e., between 2,500 to 2,620 km) has a median value of 1.9 Kpa while all deeper events (i.e., between 2,620 km and 2,800 km) exhibit a slightly smaller stress drop with a median value of 1.2 Kpa. In addition, estimation of the radius of the source ranges from 1 to 6 meters (Figure 3e) while that of the slip of fault ranges from 10^{-5} to 10^{-3} cm (Figure 3f). These results suggest that events with a larger stress drop tend to take place more often in shallower layers than in deeper layers and occur at a later time of Stage 1.2 (Figure 3b-d). Since the shallower events (occurring at a later time) exhibit a slightly larger median stress drop and a significant depth dependency effect between magnitudes and stress drops (Figure 3d), we suggest that the shallow and deep layers each have unique characteristics. To further explore the likelihood of such differences, we investigate repeating microseismic events in the next session.

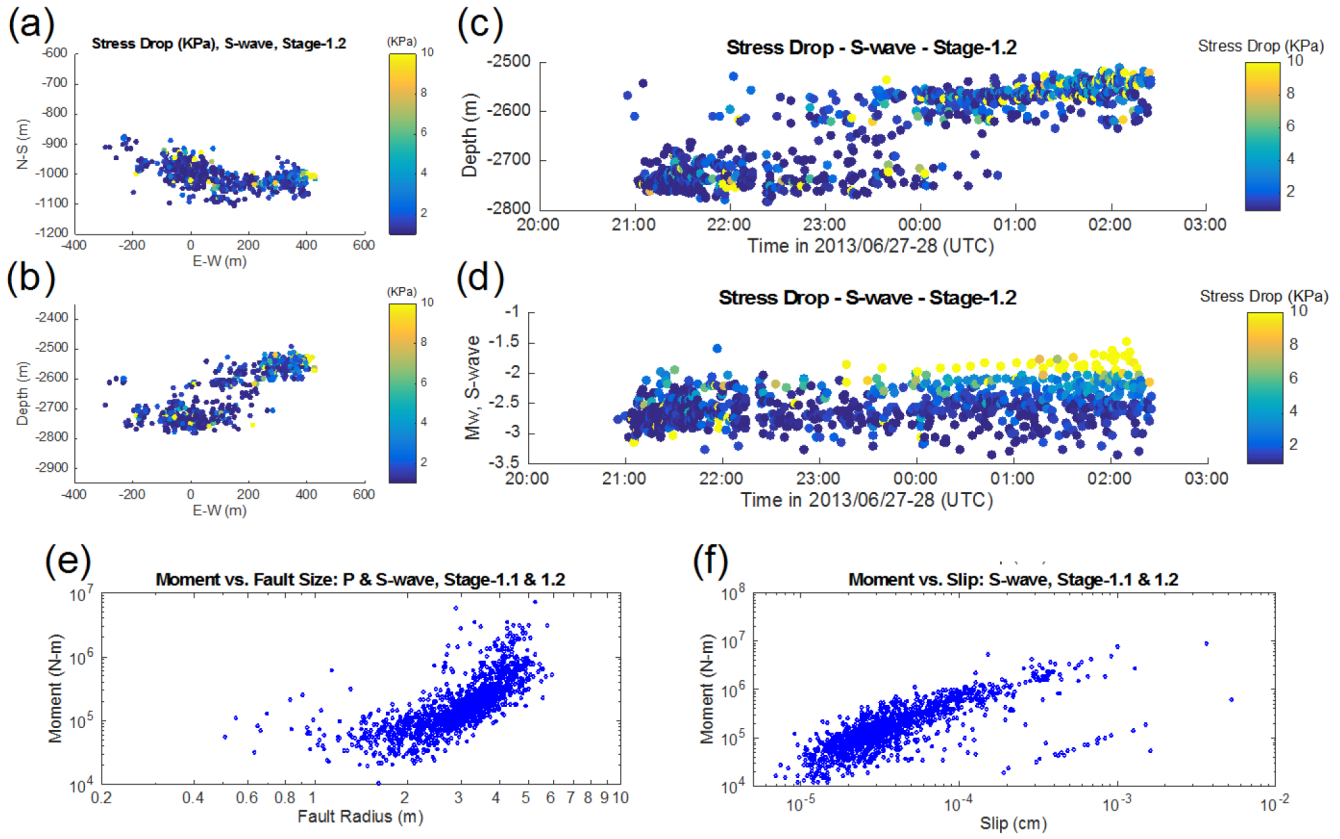

Figure 3—(a-b) Stress drop in the *S*-waves in the map (top) view and the cross section (bottom) view. (c-d) Time variation in the stress drops of *S*-waves for stage 1.2 for depth (top) and Mw (bottom). (e) Moment vs. source radius. (f) Moment versus. slip.

Detection of repeating microseismic families

To detect repeating microseismic families, we apply the waveform cross-correlation technique and identified repeating events with highly identical waveforms. We begin by cutting the time window for *P*- and *S*-waves separately for 0.03 and 0.08 sec for all 1,288 triggered events listed in the catalog. Next, we compute the cross-correlation for all combinations of all input events in each receiver component for *P*- and *S*-waves with the GISM (GI Seismology Matlab Objects, http://www.giseis.alaska.edu/Seis/EQ/tools/GISMO/) package. In other words, we identify a total of 72 (*P*- and *S*-waves, three components, and 12 receivers) outputs for repeating families.

For the final selection, the repeating families (Figures 4a-b) meet the following criteria: (1) They have highly similar waveforms with correlation coefficients greater than 0.85; (2) they contain at least three repeating events; and (3) they exhibit common events shown in at least 43 station components (i.e., higher than 60% among all detections). Once we detect a new repeating microseismic family, we stack all of the repeating waveforms and obtain waveform templates for step 3.4.

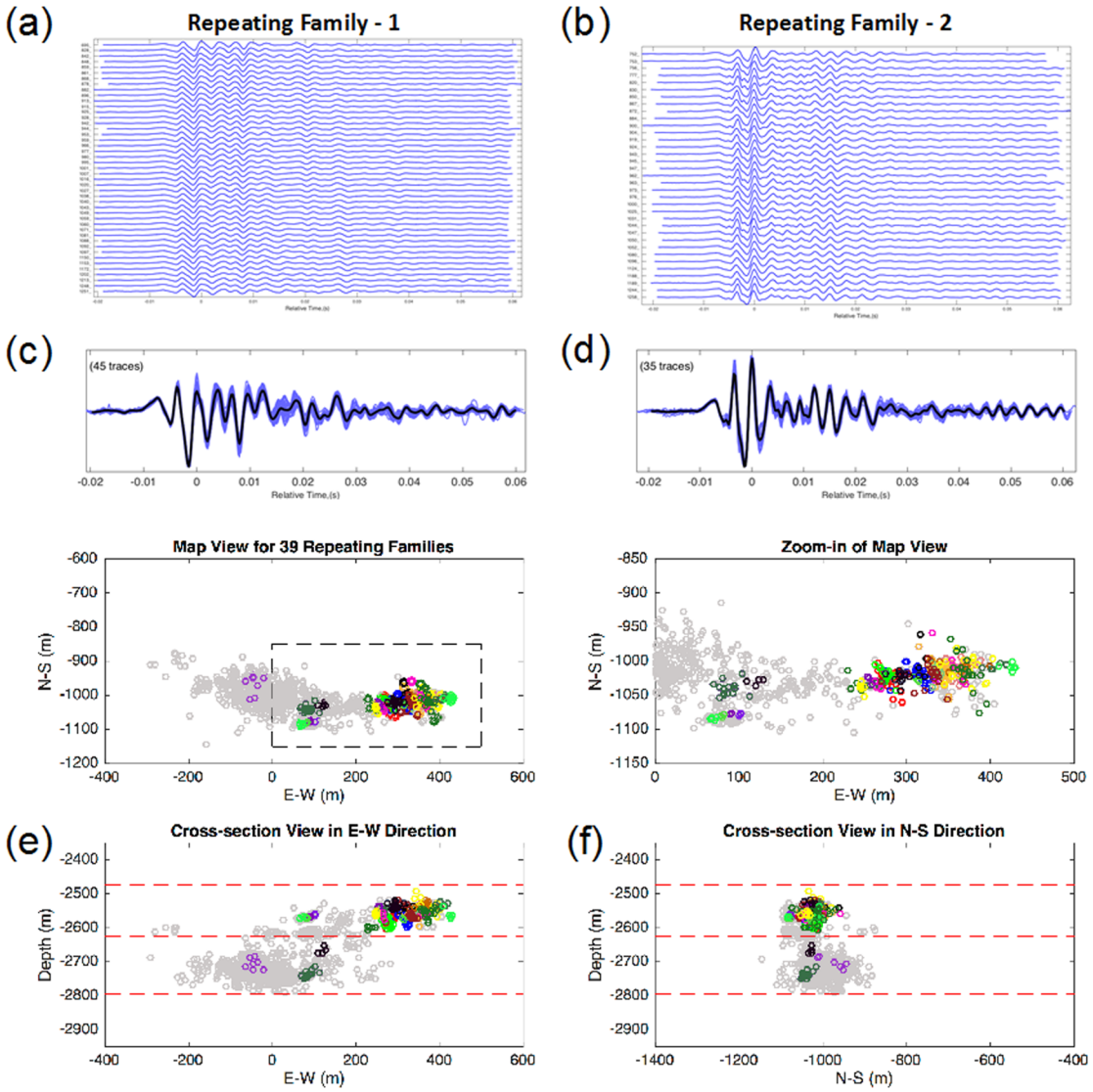

Figure 4—Example of repeating microseismic events for family #1 (a) and family #2 (b). The top panel of (a-b) shows *S*-waves from distinct events with similar waveforms in the E-component of Receiver-12. The bottom panel of (a-b) indicates stacked *S*-waves from all events in each repeating family. (c-f) The colored circles mark the locations for all 35 repeating families in the map view (c), the zoom-in of map view (d), and the cross-session view (e-f).

Of 1,288 events, we detect 35 repeating microseismic families (Figures 4c-f), each of which consists of at least three and as many as 46 repeating events. Most repeating families are located at shallower levels between 2,500 and 2,600 km deep, and they occur during a later time of stage 1.2 (Figure 4e).

In particular, we identify two types of repeating families: One is a family in which most events have similar magnitudes, and the other is one in which repeating events have different magnitudes (Figure 5). For example, the event amplitudes of repeating group #1 can be separated into two groups with large (i.e., Mw is around −2) and small magnitudes (i.e., Mw is around −2.5) (Figure 5a). These repeating events have similar waveforms (Figure 4a) but different waveform amplitudes. The spectra also show that these two groups have different amplitude spectra and corner frequencies. Despite the two magnitude groups, all of the magnitudes are proportional to the stress drop (Figure 5c).

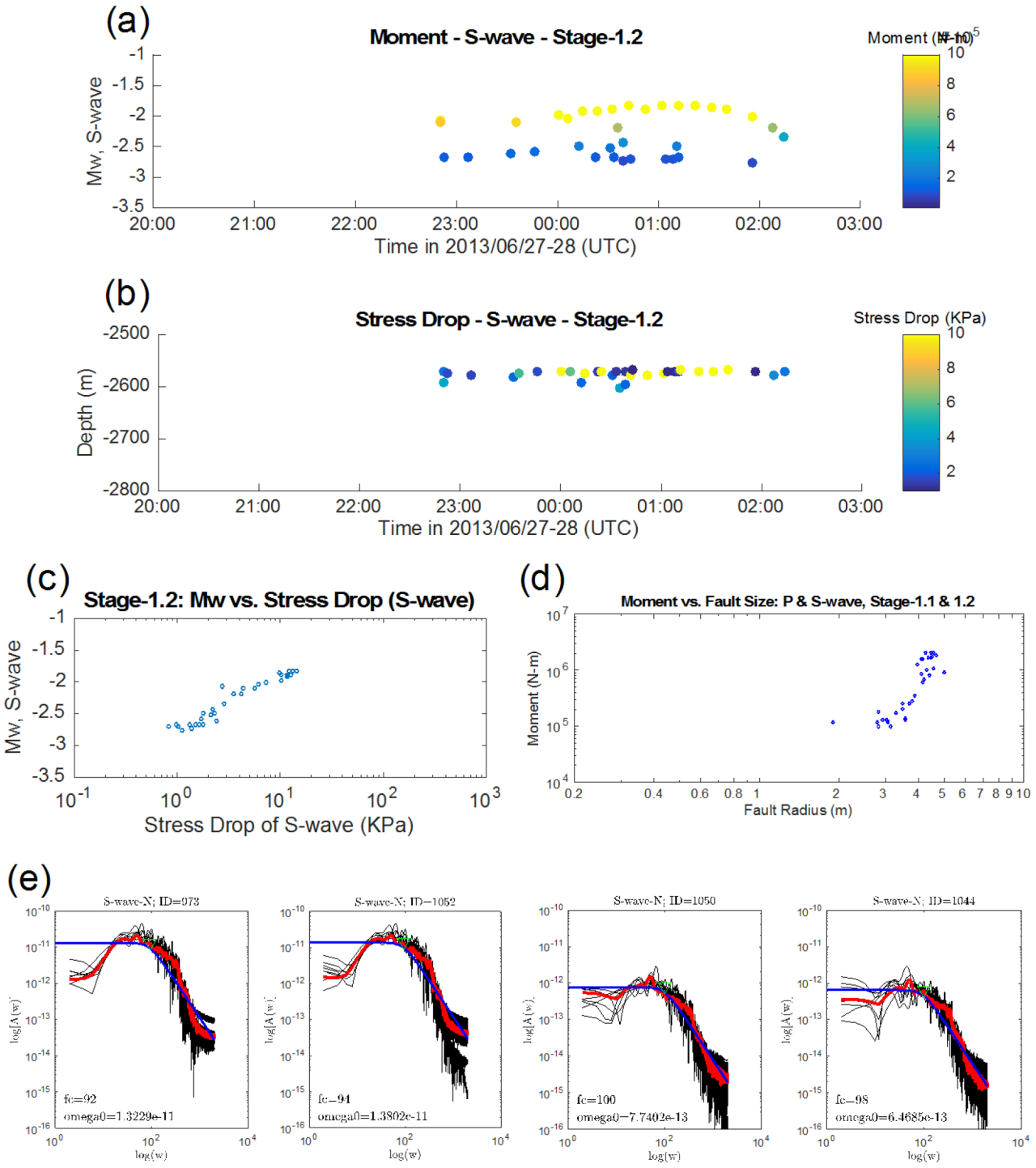

Figure 5—(a-b) The repeating microseismic events show two groups with different magnitudes. The time series show the temporal variations of magnitude (a) and depth (b). (c) The S-wave magnitudes show dependency with a stress drop. (d) The estimated fault radius for one repeating family. (e) Both groups have different amplitude spectra and corner frequencies.

Matching-filter technique for detecting new events

As we obtain repeating microseismic families, we can use the stacked waveform as the template in each station component to scan the entire dataset continuously. Through this waveform matching-filter process, we expect to detect new matched traces with a template with a highly similar waveform. We also assume that the locations of newly detected events emanate from the same spot as the repeating family because of their similar waveforms among all station-component templates (i.e., 72 templates).

In each station component, we compute the correlation coefficient (CC) values between the template waveform and ~3 hours of continuous waveforms with a shifting of one data point of the sampling rate (i.e., 4,000Hz or 1/4,000 sec per point). We adopt the same calculation for all 72 station components with the corresponding waveform templates (Figure 6a). Once we obtain the time series function of CC values for all station components, we assume that a detected event has a minimum of nine times the median CC value (Brown et al., 2008; Shelly et al., 2007) 72 receiver components. In addition, for deeper events (i.e., between 2,700 and 2,800 km) that are not included in the repeating families, we adapt the same detection procedure to confirm whether more repeating events occur in deeper sections (Figure 4e). After we apply the matching-filter technique, we detect considerably more events.

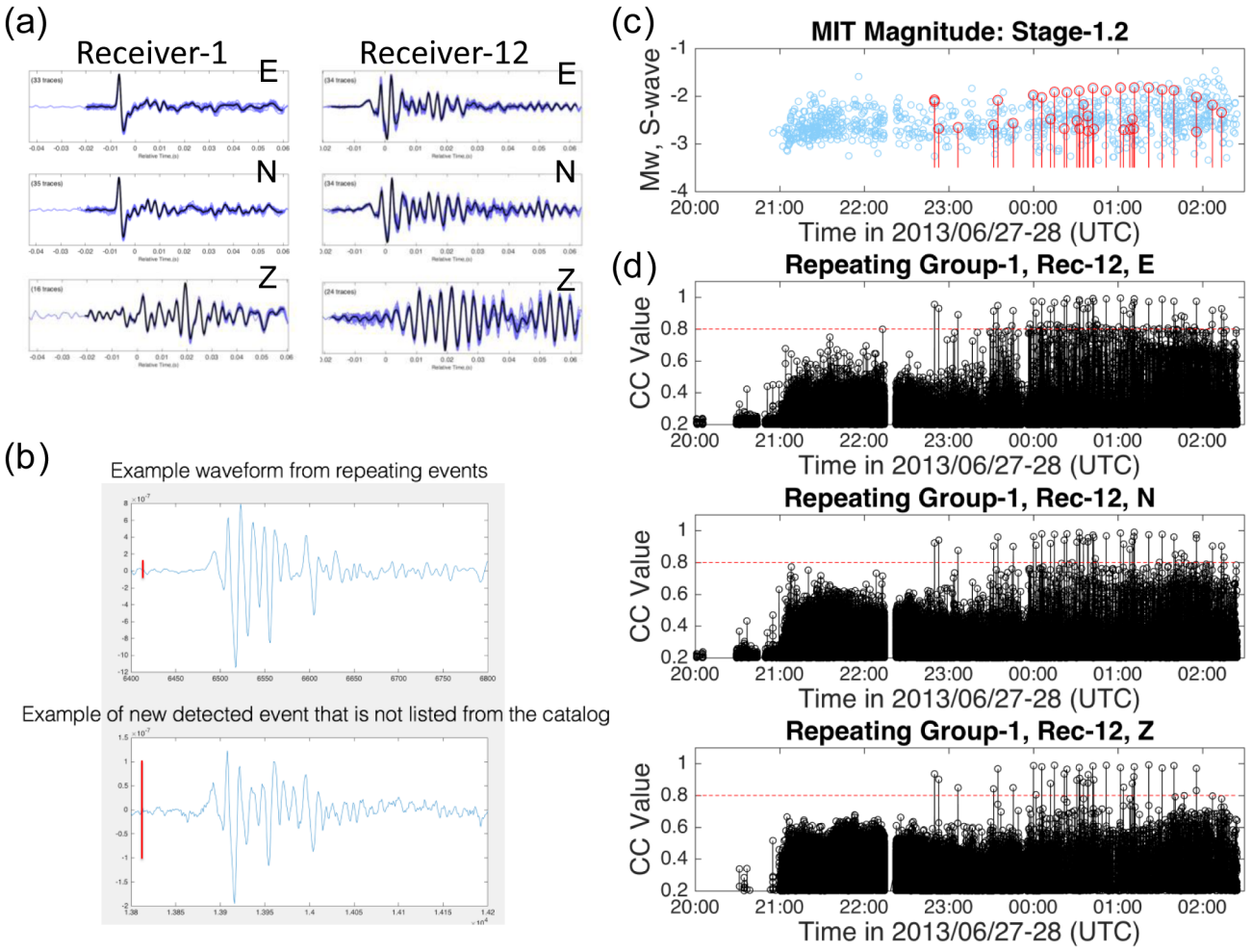

Figure 6—An example of newly detected repeating events. (a) Stacked templates show waveforms for different station components in E-, N-, and Z-components for Receivers 1, 7, and 12. (b) One template event (top) and a new detected event (bottom). The vertical red bar indicates the same length of amplitude. (c) The red circles mark all events for repeating family #1. The light blue circles show all 1,288 events in Stage 1.2. (d) Newly detected events. The red horizontal dotted lines represent a threshold of the correlation coefficient value of 0.8.

Discussion

Although the moment magnitude for the *P*- and *S*-waves show similar values, the stress drop of the *P*-waves (i.e., range from 1 to 100 KPa) shows a significantly higher value than the stress drop of the *S*-waves (i.e., range from 0.1 to 10 KPa). The weak or lack of *P*-wave arrivals could lead to an inaccurate calculation of corner frequency and moment using P-wave. On the other hand, since the *S*-waves have much larger amplitude and clear arrival times, the magnitudes and stress drop computed by them may provide more accurate information about each event. Several studies have suggested that earthquakes of various

magnitudes could have similar apparent stress (Ide and Beroza, 2001) while other studies have not observed clear stress drop dependency on the event magnitude for natural earthquakes (Chen and Shearer, 2011). In comparison, our finding suggests that small magnitude events exhibit significantly smaller stress drops. Since we use a borehole array located close to the sources of microseismic events (i.e., within 500 m), our determination could provide a better estimation of stress drop.

The current results show that most repeating families occur in the upper Vaca Muerta layers while only a few repeating events take place in the lower layers. More work needs to be done to detect much more repeated events, integrate with surface microseismic results and and other geological information to examine their location of those repeated events vs. time to improve the interpretation of the microseismic results and their relationship with the hydraulic fracture.

The new method of detecting repeating events reveals the source parameters of microseismic events with only *S*-wave arrival. Figure 6b demonstrates a newly detected repeating event with one-tenth the amplitude of the event from the catalog. With this approach we can obtain the location, the moment magnitude, the stress drop, and fault dimensions for events even without *P*-wave arrivals.

Conclusions

We have adopted a series of approaches that constrain accurate source parameters during hydraulic fracturing operations. In addition, we have obtained ~100 repeating microseismic families by applying the cross-correlation technique from these events selected from an existing microseismicity catalog. By combining repeating microseismic events and the matching-filter technique, these approaches are useful for detecting other smaller magnitude events without clear *P*-wave arrivals. These observations provide new insights that further our understanding of microseismicity related to hydraulic fracturing.

Acknowledgements

We thank Total S.A. for its financial support, and Total Austral and its partners for granting permission to publish this work.

References

Albright, J.N. and Pearson, C.F., 1982. Acoustic emissions as a tool for hydraulic fracture location: Experience at the Fenton Hill Hot Dry Rock site. *Society of Petroleum Engineers Journal*, **22**(04), 523–530. http://dx.doi.org/10.2118/9509-PA.

Anikiev, D., Valenta, J., Staněk, F., and Eisner, L., 2014. Joint location and source mechanism inversion of microseismic events: benchmarking on seismicity induced by hydraulic fracturing. *Geophysical Journal International*, **198**, 249–258. http://dx.doi.org/10.1093/gji/ggu126.

Brown, J.R., Beroza, G.C. and Shelly, D.R., 2008. An autocorrelation method to detect low frequency earthquakes within tremor. *Geophys. Res. Lett*., **35**, L16305. http://dx.doi.org/10.1029/2008GL034560.

Brune, J. N. (1970). Tectonic stress and the spectra of seismic shear waves from earthquakes. *Journal of geophysical research*, **75**(26), 4997–5009.

Caffagni, E., Eaton, D. W., Jones, J. P., & van der Baan, M. 2016. Detection and analysis of microseismic events using a Matched Filtering Algorithm (MFA). *Geopys.l J. Int*., **206**(1), 644–658.

Chen, X. and Shearer, P.M., 2011. Comprehensive analysis of earthquake source spectra and swarms in the Salton Trough, California. *J. Geophys. Res*., **116**, B09309. http://dx.doi.org/10.1029/2011JB008263.

Eisner, L., Fischer, T., and Le Calvez, J.H. 2006. Detection of repeated hydraulic fracturing (out-of-zone growth) by microseismic monitoring. *The Leading Edge*, **25**(5), 548–554. http://dx.doi.org/10.1190/1.2202655.

Eisner, L., Hulsey, B.J., Duncan, P., Jurick, D., Werner, H., and Keller, W., 2010. Comparison of surface and borehole locations of induced seismicity. *Geophysical Prospecting*, **58**(5), 809–820. http://dx.doi.org/10.1111/j.1365-2478.2010.00867.x.

Fischer, T., Hainzl, S., Eisner, L., Shapiro, S.A., and Le Calvez, J., 2008. Microseismic signatures of hydraulic fracture growth in sediment formations: Observations and modeling. *J. Geophys. Res*, **113**, B02307. http://dx.doi.org/10.1029/2007JB005070.

Gibowicz, S.J., Young, R.P., Talebi, S. and Rawlence, D.J., 1991. Source parameters of seismic events at the Underground Research Laboratory in Manitoba, Canada: Scaling relations for events with moment magnitude smaller than −2. *Bulletin of the Seismological Society of America*, **81**(4), 1157–1182.

Ide, S. and Beroza, G.C. 2001. Does apparent stress vary with earthquake size. *Geophys. Res. Lett*., **28**(17), pp.3349–3352. http://dx.doi.org/10.1029/2001GL013106.

Igarashi, T., Matsuzawa, T. and Hasegawa, A., 2003. Repeating earthquakes and interplate aseismic slip in the northeastern Japan subduction zone. *J. Geophys. Res*., **108**(B5), 2249. http://dx.doi.org/10.1029/2002JB001920.

Kane, D. L., Prieto, G. A., Vernon, F. L., & Shearer, P. M. (2011). Quantifying seismic source parameter uncertainties. *Bulletin of the Seismological Society of America*, **101**(2), 535–543.

Nadeau, R.M. and Johnson, L.R., 1998. Seismological studies at Parkfield VI: Moment release rates and estimates of source parameters for small repeating earthquakes. *Bulletin of the Seismological Society of America*, **88**(3), 790–814.

Peng, Z. and Zhao, P., 2009. Migration of early aftershocks following the 2004 Parkfield earthquake. *Nature Geoscience*, **2**(12), 877–881. http://dx.doi.org/10.1038/ngeo697.

Prieto, G. A., Thomson, D. J., Vernon, F. L., Shearer, P. M., & Parker, R. L. (2007). Confidence intervals for earthquake source parameters. *Geophysical Journal International*, **168**(3), 1227–1234.

Shearer, P.M., 2009. *Introduction to seismology*. Cambridge University Press.

Shelly, D.R., Beroza, G.C., and Ide, S., 2007. Non-volcanic tremor and low-frequency earthquake swarms. *Nature*, **446**, 305–307. http://dx.doi.org/10.1038/nature05666.

Stein, S. and Wysession, M. 2009. An introduction to seismology, earthquakes, and earth structure. John Wiley & Sons.

Stuermer, K., Kummerow, J., and Shapiro, S.A. 2012, November. Multiplet based extraction of geological structures. *2012 SEG Annual Meeting*, Las Vegas, Nevada, 4-9 November, SEG-2012-1048.

Uchida, N., Iinuma, T., Nadeau, R.M., Bürgmann, R., and Hino, R. 2016. Periodic slow slip triggers megathrust zone earthquakes in northeastern Japan. *Science*, **351**, 488–492. http://dx.doi.org/10.1126/science.aad3108.

Warpinski, N., 2009. Microseismic monitoring: Inside and out. *Journal of Petroleum Technology*, **61**(11), 80–85. http://dx.doi.org/10.2118/118537-JPT.